

A Multi-Fidelity Tensor Emulator for Spatiotemporal Outputs: Emulation of Arctic Sea Ice Dynamics

Tristan Contant^{1*} Yawen Guan^{1 †} Ander Wilson¹ Adrian K. Turner²
Deborah Sulsky³

¹Department of Statistics, Colorado State University

²Los Alamos National Laboratory

³Department of Mathematics and Statistics, University of New Mexico

Abstract

Numerical models are widely used to simulate the earth system, but they are computationally expensive and often depend on many uncertain input parameters. Their effective use requires calibration and uncertainty quantification, which typically involve running the model across many input configurations and therefore incur substantial computational cost. Statistical emulation provides a practical alternative for efficiently exploring model behavior. We are motivated by the Arctic sea ice component of the Energy Exascale Earth System Model (MPAS-Seaice), which generates large spatiotemporal outputs at multiple spatial resolutions, with high-resolution (or high-fidelity, HF) simulations being more accurate but computationally more expensive than lower-resolution (low-fidelity, LF) simulations. Multi-fidelity (MF) emulation integrates information across resolutions to construct efficient and accurate surrogate models, yet existing approaches struggle to scale to large spatiotemporal data. We develop an MF emulator that combines tensor decomposition for dimensionality reduction, Gaussian process priors for flexible function approximation, and an additive discrepancy model to capture systematic differences between LF and HF data. The proposed framework enables scalable emulation while maintaining accurate predictions and well-calibrated uncertainty for complex spatiotemporal fields, and consistently achieves lower prediction error and reduced uncertainty than LF-only and HF-only models in both simulation studies and MPAS-Seaice analysis. By leveraging the complementary strengths of LF and HF data and using an efficient tensor decomposition approach, our emulator greatly reduces computational expense, making it well suited for large-scale simulation tasks involving complex physical models.

Keywords: surrogate modeling; Tucker decomposition; dimensionality reduction; Gaussian process; earth system modeling

*Tristan.Contant@colostate.edu

†Yawen.Guan@colostate.edu

1 Introduction

Numerical models are widely used to simulate the earth system and study the complex physical processes that drive variability across interacting atmospheric, oceanic, terrestrial, and cryospheric components (Chen et al., 2021). Within this interconnected system, Arctic sea ice is a critical component that regulates ocean-atmosphere exchanges, influences large-scale circulation, and supports polar ecosystems, while also affecting human activities such as coastal communities and marine navigation (Stroeve and Notz, 2018). Accurately representing sea ice dynamics in numerical models requires careful parameterization and tuning, as well as simulations at sufficiently high spatial resolution to resolve key physical and biogeochemical processes and localized phenomena (Blockley et al., 2020). However, high-resolution model simulations are computationally expensive, severely limiting the number of parameter combinations that can be explored (Schneider et al., 2017). To address these challenges, statistical emulators offer efficient alternatives that enable broader exploration of parameter space and improved uncertainty quantification, while substantially reducing computational cost (Sudakow et al., 2022).

MPAS-Seaice (Turner et al., 2022) is the sea-ice component of the Energy Exascale Earth System Model (E3SM; Leung et al., 2020), the U.S. Department of Energy’s Earth System Model. The model includes a comprehensive representation of sea ice physics, including vertical thermodynamics based on mushy layer physics (Turner and Hunke, 2015), shortwave radiation penetration and absorption (Briegleb and Light, 2007), sea ice biogeochemistry (Jeffery et al., 2020), tracer transport (Lipscomb and Hunke, 2004), melt ponds (Hunke et al., 2013), ridging and mechanical redistribution (Lipscomb et al., 2007), and solution of the sea ice momentum equation (Turner et al., 2022). The model is forced by atmospheric and oceanic fields—such as winds, ocean currents, temperature, radiation, and sea surface conditions—that drive thermodynamic and dynamic evolution of the sea ice (Urrego-Blanco et al., 2016). MPAS-Seaice is a key modeling tool for advancing the scientific understanding of sea-ice dynamics and thermodynamics. As part of the E3SM model, MPAS-Seaice supports a wide range of research efforts, from evaluating coupled earth-system interactions to informing model development and assessment across the scientific community (Leung et al., 2020; Turner et al., 2022).

For a given set of geophysical input parameters, MPAS-Seaice produces output describing the evolution of the sea-ice state over time on an unstructured spherical centroidal Voronoi tessellation of the sphere, provided by the Model for Prediction Across Scales (MPAS; Ringer et al., 2010) modeling framework. Typically, MPAS-Seaice is run repeatedly over many different input parameter settings for model tuning purposes, producing output fields over space and time that together form a tensor. MPAS-Seaice can be run at multiple spatial resolutions. Finer spatial resolution (henceforth high-fidelity or HF) captures small-scale processes like lead formation (openings in the ice) but is computationally expensive, limiting how many HF simulations can be performed. Coarse-resolution simulations (henceforth low-fidelity or LF) are cheaper and allow many more runs, but they can miss important fine-scale dynamics. As a result, simulations at different fidelities are not simply related by interpolation; they exhibit systematic differences in their representation of sea-ice processes. In this work, our goal is to leverage both LF and HF outputs to emulate MPAS-Seaice at high-resolution for new inputs, while rigorously quantifying associated uncertainties.

Several methods exist for emulating scalar-valued outcomes, including polynomial chaos expansions (O’Hagan, 2013), neural networks (Haykin, 1998), support vector machines (Smola and Schölkopf, 2004), and Gaussian processes (GPs) (Sacks et al., 1989). In particular, GPs are widely used for modeling spatial and temporal data due to their inherent flexibility and uncertainty quantification (Cressie, 1993). However, when the data span many spatiotemporal locations, GP emulation becomes computationally infeasible (Rasmussen and Williams, 2006). To address this,

basis decomposition methods—such as principal component analysis (PCA) (Higdon et al., 2008; Ekanayaka et al., 2025), splines (Bowman and Woods, 2016), radial basis functions (Yi et al., 2020), and Fourier functions (Partovizadeh et al., 2025)—represent outputs as combinations of basis functions and associated weights, reducing the emulation task to modeling the weights. While these dimensionality reduction techniques improve computational feasibility, they either require the *a priori* selection of spatial and/or temporal basis functions to represent variability, or rely on vectorizing spatiotemporal outputs; both limit the ability to capture complex spatiotemporal interactions (Kiers and Van Mechelen, 2001; Anandkumar et al., 2016; Ju et al., 2018; Zare et al., 2018).

None of the aforementioned methods integrate multiple resolutions from a simulator like MPAS-Seaice. Simply interpolating LF output onto the HF grid (e.g., with nearest-neighbor or linear interpolation) only increases spatial resolution and does not correct for systematic differences between different fidelities, such as numerical errors, unresolved physics, or structural model biases. These discrepancies remain regardless of interpolation, motivating a more principled way to combine information across resolutions. Multi-fidelity (MF) emulators use inexpensive LF simulations together with a limited number of HF runs to achieve accurate predictions while avoiding the cost of extensive HF simulations (Forrester et al., 2007; Fernández-Godino, 2023). To account for systematic differences between fidelities, Kennedy and O’Hagan (2000) proposed an additive discrepancy model that expresses HF output as the sum of LF output and a discrepancy term. This approach has since been widely adopted across a variety of applications (e.g., Huang et al., 2013; Roderick et al., 2014; Liu et al., 2022; Ma et al., 2022; Bird et al., 2023). However, capturing a high-dimensional, spatiotemporally structured, and input-dependent discrepancy term remains challenging. Dimension reduction approaches based on predefined basis functions or PCA likewise have limited ability to represent important spatiotemporal interactions.

We develop a novel MF emulator that integrates tensor decomposition for dimension reduction with an additive discrepancy model to jointly utilize MPAS-Seaice simulations at two fidelity levels. Specifically, we employ Tucker decomposition to represent the spatiotemporal model output in a reduced-dimensional tensor space, allowing mode-specific compression across space and time (Tucker, 1966). Unlike other basis decompositions, Tucker decomposition preserves the intrinsic tensor structure of the data and more flexibly captures interactions across spatial and temporal modes. The resulting dimensionality reduction substantially improves computational efficiency by restricting emulation to a small set of coefficients, for which we place independent GP priors. By explicitly learning the discrepancy between fidelity levels, our method leverages inexpensive LF runs together with a limited number of HF simulations to produce accurate, high-resolution predictions with rigorous uncertainty quantification. This work represents the first application of MF emulation to tensor-valued outputs and is the first to emulate the spatiotemporal outputs of MPAS-Seaice. This approach enables more extensive and scalable studies of sea-ice behavior across multiple fidelities.

The remainder of this paper is organized as follows. Section 2 describes the MPAS-Seaice model and the simulation ensembles used for emulation. Section 3 introduces the proposed multi-fidelity tensor emulator, beginning with a single-fidelity tensor emulator applicable to numerical models with spatiotemporal outputs and then extending it to the multi-fidelity setting. Section 4 presents results from a simulation study, and Section 5 applies the method to MPAS-Seaice data, comparing the proposed approach with LF- and HF-only alternatives and a baseline model. Section 6 concludes with a discussion of potential extensions and directions for future research.

2 Data

MPAS-Seaice produces several output variables that characterize sea-ice behavior, including sea ice area, volume, and velocity. In this study, we focus on sea ice area. We conducted simulations using E3SM version 3.0.2 (E3SM Project, 2024) in standalone mode for the Northern Hemisphere and forced the model with six-hourly atmospheric fields for air temperature, air specific humidity, and 10m air velocity from the JRA-3Q reanalysis (Kosaka et al., 2024), along with monthly climatologies of cloudiness (Röske, 2001) and precipitation (Griffies et al., 2009). Downwelling shortwave radiation was calculated from cloudiness using the Arctic Ocean Model Intercomparison Project shortwave forcing formula (Hunke et al., 2015), while downwelling longwave radiation was calculated following Rosati and Miyakoda (1988). Oceanic forcing inputs of sea surface salinity, initial sea surface temperature, currents, deep ocean heat flux, and sea-surface gradient were obtained from a monthly mean of 20 years of a Community Climate System Model climate run (Collins et al., 2006).

We ran MPAS-Seaice on two quasi-uniform MPAS meshes covering the Arctic ocean and surrounding seas at spatial resolutions of 60 km and 30 km, corresponding to the LF and HF configurations. These resolutions were selected to balance scientific validity with computational feasibility. The finer 30 km mesh provided higher physical fidelity, more accurately representing small-scale processes such as sea-ice deformation. The 60 km mesh provided a coarser but still scientifically meaningful representation of large-scale processes; meshes coarser than 60 km failed to resolve key physical processes. Simulations on these meshes yielded $n_s^{\text{LF}} = 11,661$ spatial locations, corresponding to mesh cell centers, for LF and $n_s^{\text{HF}} = 33,530$ for HF. While we considered two fidelity levels, the methodology developed here can be generalized to accommodate multiple fidelity levels.

Figure 1 compares MPAS-Seaice runtimes for the two spatial configurations on the National Energy Research Scientific Computing Center (NERSC) Perlmutter high performance computing system (Lockwood et al., 2021). At 16 processors, the LF configuration took roughly three times longer than the HF configuration. The LF model showed diminishing speedup at higher processor counts while the HF model continued to scale efficiently. At 256 processors, HF runtimes were comparable to LF runtimes using fewer than 16 processors, implying that LF simulations can reduce computational cost by up to a factor of 16. This difference in computational cost motivates the development of an emulator for MPAS-Seaice that leverages both fidelity levels, not solely relying on HF simulations.

We ran MPAS-Seaice ensembles over a range of input settings; among all model inputs, we varied six highly sensitive parameters selected based on sensitivity analyses reported in Urrego-Blanco et al. (2016), with prior distributions also informed by that study. We denote these input parameters by a $p = 6$ dimensional vector \mathbf{x} , consisting of thermal conductivity of snow, neutral ocean-ice drag, drainage time scale of ponds, two parameters controlling snow grain size, and solid fraction at the ice-ocean interface. The LF design set $\mathcal{X}^{\text{LF}} = \{\mathbf{x}_1, \dots, \mathbf{x}_{n_x^{\text{LF}}}\}$, with $n_x^{\text{LF}} = 89$, was generated via Latin Hypercube Sampling with a maximin criterion, and inputs were transformed to physical units via the inverse CDFs of their respective priors. A subset $\mathcal{X}^{\text{HF}} \subset \mathcal{X}^{\text{LF}}$ of size $n_x^{\text{HF}} = 21$ was selected for the HF design points. Our approach remains applicable when the designs are non-nested.

For each input, MPAS-Seaice was configured to produce output every ten days, which we averaged to monthly for analysis. Each simulation spanned 1976–2009, with the first 23 years treated as spin-up to remove sensitivity to initial conditions and the remaining 11 years used for emulation. Consequently, each sea ice area output field was represented as a third-order tensor with modes corresponding to spatial location, month, and year. By including both monthly and yearly temporal modes, we explicitly captured seasonal and interannual variability. For each spatial resolution,

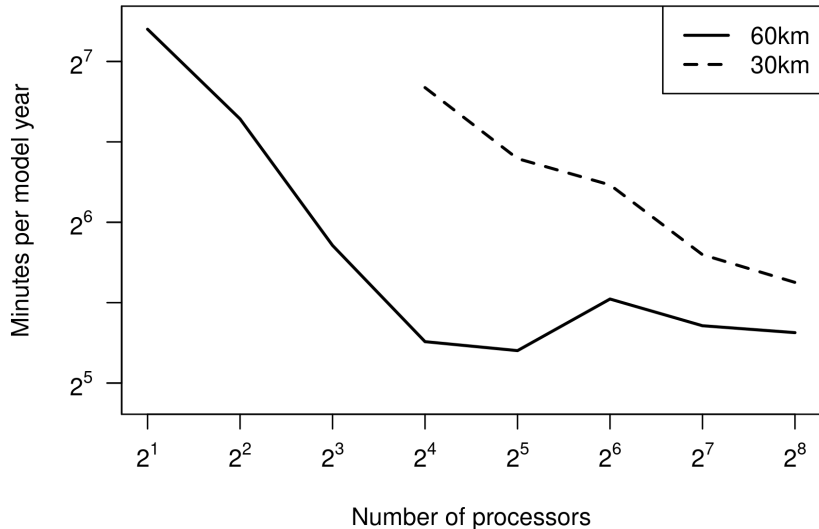


Figure 1: Run time comparison for 60 km (low-fidelity, LF) and 30 km (high-fidelity, HF) MPAS-Seaice simulations. The HF model is slower at low processor counts but benefits more from additional processors, while the LF model shows diminishing speedup. LF simulations are up to 16 times cheaper in computational cost than the HF simulations.

outputs corresponding to different input settings were stacked into a fourth-order tensor, with the final mode indexing the design space. See Supplementary Figures S1 and S2 for representative temporal trends and example spatial fields of sea ice area output from MPAS-Seaice, respectively.

We aim to develop a methodology that is broadly applicable to spatiotemporal output fields commonly produced by numerical models, regardless of their marginal support. We evaluate the proposed approach using sea-ice area, defined as the proportion of a grid cell covered by sea ice at a given time and naturally bounded between 0 (no ice) and 1 (full coverage). To accommodate this bounded variable within a general emulation framework, we propose a monotone nondecreasing transformation that maps the data to the real line without altering its essential spatiotemporal structure. The transformation is necessary since basis decomposition methods such as PCA or Tucker decomposition yield representations with support on the real line and may otherwise produce invalid values when applied directly to bounded data (Giordani and Kiers, 2007). In addition, the transformation facilitates direct comparison with existing emulation methods developed for unconstrained outputs. Specifically, we utilized a logit-based transformation to the sea-ice area. First, we clipped values to the interval $[0.01, 0.99]$ to ensure the logit is well-defined. We then applied the transformation

$$f(x) = \text{logit} \left[\frac{\exp(x/\epsilon) - 1}{\exp(1/\epsilon) - 1} \right]$$

where a smoothing parameter $\epsilon = 10^{-3}$ pulls values near the boundaries toward the clipped limits (0.01 and 0.99), producing a near-linear mapping over the interior range (see Figure 2). This transformation maps the bounded $[0, 1]$ data to the real line, enabling the use of standard decomposition techniques such as PCA or Tucker decomposition. Emulator predictions are mapped back to $[0, 1]$ using the inverse transformation. This approach outperforms a logit-only transform, avoiding distortions in transition zones between high and low sea-ice area.

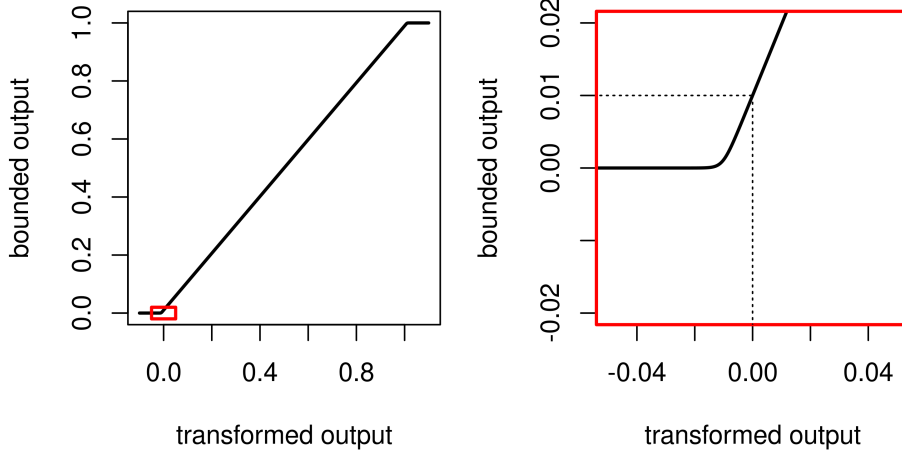


Figure 2: Logit-based transformation of $[0, 1]$ -bounded MPAS-Seaice outputs to the real line. Values are truncated to $[0.01, 0.99]$ and then mapped using a compressed logit function, resulting in a near-linear mapping between 0.1 and 0.99. The left panel shows the full transformation, and the right panel a zoomed-in view. This ensures that the data are suitable for the proposed methodology, which is broadly applicable to real-valued data and enables the use of basis decomposition methods such as Tucker decomposition.

3 Methods

We first introduce a framework for emulating single-fidelity tensor output in Section 3.1, and then present the multi-fidelity tensor emulator in Section 3.2. Motivated by the MPAS-Seaice data, we consider simulator tensor output that is third-order (spatial location, month, and year) and, in the MF case, has two fidelities. The methods presented can be extended to tensors with an arbitrary number of modes and more than two fidelities.

3.1 Single-Fidelity Tensor Emulation

Let $M(\cdot)$ denote a deterministic computer model mapping $\mathbf{x} \in \mathbb{R}^p$ to a spatiotemporal output $M(\mathbf{x}) \in \mathbb{R}^{n_s \times n_m \times n_y}$, where n_s is the number of spatial locations, n_m is the number of temporal points per year (e.g., months), and n_y is the number of years. The total number of spatiotemporal points is $n = n_s n_m n_y$. Combining the emulator output tensors for a set of n_x design points $\mathcal{X} = \{\mathbf{x}_1, \dots, \mathbf{x}_{n_x}\}$, we form the tensor $\mathcal{Z} \in \mathbb{R}^{n_s \times n_m \times n_y \times n_x}$. Our objective is to train an emulator $\eta(\mathbf{x}^*)$ that predicts $M(\mathbf{x}^*)$ at new inputs $\mathbf{x}^* \notin \mathcal{X}$ and characterizes uncertainty in its predictions. While we focus on a single spatiotemporal output variable here, multiple outputs of interest can be accommodated by augmenting the representation with an additional tensor mode corresponding to the output index.

3.1.1 Emulation via Tucker Tensor Decomposition

For a single fidelity, we construct a tensor emulator via basis function representation with basis functions $\mathcal{B}_{j_s j_m j_y} \in \mathbb{R}^{n_s \times n_m \times n_y}$ and weights $w_{j_s j_m j_y}(\mathbf{x}) \in \mathbb{R}$ as

$$\eta(\mathbf{x}) = \sum_{j_s=1}^{r_s} \sum_{j_m=1}^{r_m} \sum_{j_y=1}^{r_y} \mathcal{B}_{j_s j_m j_y} w_{j_s j_m j_y}(\mathbf{x}) + \mathcal{E}_\eta, \quad (1)$$

where r_s , r_m , and r_y denote the number of spatial, monthly, and yearly basis components, respectively. Each basis is a $n_s \times n_m \times n_y$ tensor that captures spatiotemporal structure, while the corresponding weights vary over the design space. Approximation error is represented by $\epsilon_\eta = \text{vec}(\mathcal{E}_\eta) \sim \mathcal{N}(\mathbf{0}, \lambda_\eta^{-1}I)$ with precision λ_η .

We train the emulator in (1) using the ensemble of training runs \mathcal{Z} . To obtain a low-dimensional representation of these training outputs, we compute a truncated Tucker decomposition of \mathcal{Z} ,

$$\mathcal{Z} \approx \mathcal{G} \times_1 U_s \times_2 U_m \times_3 U_y \times_4 U_x,$$

where \times_k is the mode- k tensor-matrix product (Tucker, 1966). The factor matrices $U_s \in \mathbb{R}^{n_s \times r_s}$, $U_m \in \mathbb{R}^{n_m \times r_m}$, $U_y \in \mathbb{R}^{n_y \times r_y}$, and $U_x \in \mathbb{R}^{n_x \times r_x}$ have orthonormal columns and provide mode-specific bases for space, month, year, and the design index, respectively. The core tensor $\mathcal{G} \in \mathbb{R}^{r_s \times r_m \times r_y \times r_x}$ captures interactions among these mode-specific bases. Allowing (r_s, r_m, r_y, r_x) to differ is important in our applications because the complexity of the simulator output can vary by mode. In contrast, canonical polyadic decomposition of tensors imposes a shared rank across modes (Kolda and Bader, 2009).

Tucker decomposition induces a basis-weight representation that matches (1). For (j_s, j_m, j_y) , define the basis tensor and the corresponding data-derived weight at design point \mathbf{x}_i as

$$\begin{aligned} \mathcal{B}_{j_s j_m j_y} &= U_s[:, j_s] \circ U_m[:, j_m] \circ U_y[:, j_y], \\ \hat{w}_{j_s j_m j_y}(\mathbf{x}_i) &= \sum_{j_x=1}^{r_x} \mathcal{G}[j_s, j_m, j_y, j_x] U_x[i, j_x], \end{aligned} \quad (2)$$

where \circ denotes the outer product and bracket notation indexes tensor elements. Collecting $\hat{w}_{j_s j_m j_y}(\mathbf{x}_i)$ over all i yields an observed weight tensor $\hat{\mathcal{W}} \in \mathbb{R}^{n_x \times r_s \times r_m \times r_y}$ and vector $\hat{\mathbf{w}} = \text{vec}(\hat{\mathcal{W}})$. We treat these $\hat{\mathbf{w}}$ as weights implied by the finite-rank approximation of the observed data \mathcal{Z} , and distinguish them with hats from the latent weight functions $w_{j_s j_m j_y}(\mathbf{x})$ in (1) that are modeled over \mathbf{x} . We do not place hats on the basis tensors $\mathcal{B}_{j_s j_m j_y}$ because, following common practice in reduced-rank GP emulation and PCA/basis-function emulation, we adopt a plug-in approach: the bases obtained from the Tucker decomposition are treated as fixed (empirical) quantities during subsequent inference, while uncertainty is propagated through the input-dependent weight processes.¹

Crucially, the dependence on \mathbf{x}_i enters (2) only through the columns of U_x . Write $U_x[:, j_x] = \hat{\gamma}_{j_x}$ and refer to these columns as *effective weights*. Let $\hat{\boldsymbol{\gamma}} = \text{vec}(U_x)$ be the vectorized collection of all effective weights. Then the full observed weights are a fixed linear transformation of the effective weights,

$$\hat{\mathbf{w}} = \left(G_{(4)}^\top \otimes I_{n_x} \right) \hat{\boldsymbol{\gamma}} := T \hat{\boldsymbol{\gamma}}, \quad (3)$$

where $G_{(4)}$ is the mode-4 unfolding of \mathcal{G} and \otimes is the Kronecker product. Consequently, it is sufficient to emulate the r_x latent effective-weight processes $\{\gamma_{j_x}(\mathbf{x})\}$; predictions of the full coefficient set $\{w_{j_s j_m j_y}(\mathbf{x})\}$ for new inputs are obtained by applying the same mapping T .

The ranks (r_s, r_m, r_y, r_x) control the reduction of the data, with lower ranks producing a more compact representation (i.e., fewer bases). We select the ranks by performing PCA on each mode-unfolding of \mathcal{Z} and selecting the smallest rank that captures a preset fraction of the total variance. Then, the core tensor and factor matrices are obtained using Higher-Order Orthogonal Iteration

¹Some papers explicitly denote estimated bases with hats (e.g., $\hat{\mathcal{B}}$) to emphasize that they are learned from the training ensemble; others omit the hats once the basis is fixed. We follow the latter convention to keep notation light, and reserve hats for quantities (weights) that are directly treated as noisy observations of latent functions over \mathbf{x} .

(HOOI), a block coordinate descent algorithm that produces orthonormal factors and locally minimizes the approximation error (De Lathauwer et al., 2000). For given ranks, HOOI of a d -way tensor converges to a decomposition with an approximation error that is within \sqrt{d} of the true minimum approximation error (Ballard and Kolda, 2025). We implement HOOI using the `rTensor` package (Li et al., 2018).

3.1.2 Probability Model and Posterior Inference

Given the bases and weights in (2), emulation reduces to modeling the effective weights γ_{j_x} over the design space. Because the r_x columns of U_x are orthogonal, we place independent GP priors on each effective weight γ_{j_x} for $j = 1, \dots, r_x$. The GP priors are mean zero with an anisotropic exponential kernel parameterized by a precision and length scales. Let $\Sigma_{\gamma_{j_x}}(\mathcal{X}, \mathcal{X})$ denote the covariance matrix corresponding to effective weight γ_{j_x} , evaluated over all pairwise comparisons of the design points in \mathcal{X} . The GP priors for all effective weights can then be combined into a prior with covariance $\Sigma_\gamma(\mathcal{X}, \mathcal{X}) = \text{blockDiag}[\Sigma_{\gamma_1}(\mathcal{X}, \mathcal{X}), \dots, \Sigma_{\gamma_{r_x}}(\mathcal{X}, \mathcal{X})]$.

With basis functions, GP priors on the effective weights, and approximation error, the Bayesian hierarchical model is

$$\begin{aligned} \mathbf{z} \mid \boldsymbol{\gamma}, \lambda_\eta &\sim \mathcal{N}(BT\boldsymbol{\gamma}, \lambda_\eta^{-1}I) \\ \boldsymbol{\gamma} &\sim \mathcal{N}(\mathbf{0}, \Sigma_\gamma(\mathcal{X}, \mathcal{X})) \\ \lambda_\eta &\sim \Gamma(a_\eta, b_\eta) \end{aligned} \quad (4)$$

where $\mathbf{z} = \text{vec}(\mathcal{Z})$ is the vectorized collection of outputs, $\mathbf{b}_{j_s j_m j_y} = \text{vec}(\mathcal{B}_{j_s j_m j_y}) \in \mathbb{R}^n$ are the vectorized basis tensors, and $B = [I_{n_x} \otimes \mathbf{b}_{111}, \dots, I_{n_x} \otimes \mathbf{b}_{r_s r_m r_y}]$. The model in (4) can be reduced by condensing the information in \mathbf{z} to the observed set of effective weights $\hat{\boldsymbol{\gamma}}$ and integrating out the latent effective weights $\boldsymbol{\gamma}$ (Higdon et al., 2008). This yields

$$\begin{aligned} \hat{\boldsymbol{\gamma}} \mid \lambda_\eta &\sim \mathcal{N}\left(\mathbf{0}, \lambda_\eta^{-1}(C^\top C)^{-1} + \Sigma_\gamma(\mathcal{X}, \mathcal{X})\right) \\ \lambda_\eta &\sim \Gamma(a'_\eta, b'_\eta), \end{aligned} \quad (5)$$

where $C = BT$, $a'_\eta = a_\eta + d(n - r_x)/2$ and $b'_\eta = b_\eta + \mathbf{z}^\top [I - C(C^\top C)^{-1}C^\top] \mathbf{z}/2$. In (5), C has a sparse structure that we leverage to improve computational efficiency. See Supplementary Materials A.1 and A.3 for a detailed derivation of (5) and for the calculation of $C^\top C$ and $C^\top \mathbf{z}$, respectively.

Samples from the posterior distribution of the model in (5) are obtained using a Markov chain Monte Carlo (MCMC) algorithm with Metropolis Hastings (HF) updates (see Supplementary Material B for additional details). We place an independent folded-normal prior with location 0 and scale 1 on the GP precision and independent log-normal prior with location 0 and scale 1 on the length scale parameters. For the Γ prior on λ_η , we set $a_\eta = 1$ and $b_\eta = 1/2$.

3.1.3 Emulation via Posterior Prediction

Emulator η predicts $M(\mathbf{x}^*)$ at new inputs $\mathbf{x}^* \notin \mathcal{X}$. From the joint distribution of the observed and unobserved effective weights,

$$\begin{bmatrix} \hat{\boldsymbol{\gamma}} \\ \boldsymbol{\gamma}^* \end{bmatrix} \sim \mathcal{N}\left(\mathbf{0}, \begin{bmatrix} \lambda_\eta^{-1}(C^\top C)^{-1} + \Sigma_\gamma(\mathcal{X}, \mathcal{X}) & \Sigma_\gamma(\mathcal{X}, \mathbf{x}^*) \\ \Sigma_\gamma(\mathbf{x}^*, \mathcal{X}) & \Sigma_\gamma(\mathbf{x}^*, \mathbf{x}^*) \end{bmatrix}\right),$$

we derive the conditional distribution of $\boldsymbol{\gamma}^*$ given $\hat{\boldsymbol{\gamma}}$ via standard multivariate normal results. For each posterior predictive draw of $\boldsymbol{\gamma}^*$ from this conditional distribution, the full spatiotemporal prediction is obtained by $\text{vec}[\eta(\mathbf{x}^*)] = B_\eta G_{(4)}^\top \boldsymbol{\gamma}^* + \boldsymbol{\epsilon}_\eta$, where $B_\eta = [\mathbf{b}_{111}, \dots, \mathbf{b}_{r_s r_m r_y}]$.

3.2 Multi-Fidelity Tensor Emulation

We extend the single-fidelity emulator from Section 3.1 to an MF setting using two simulators of differing spatial resolution. The LF simulator $M^{\text{LF}}(\mathbf{x})$ runs on n_s^{LF} spatial locations, while the HF simulator $M^{\text{HF}}(\mathbf{x})$ uses a finer grid with n_s^{HF} locations. We do not require the spatiotemporal points to be nested across fidelities. Let $n^{\text{LF}} = n_s^{\text{LF}} n_m n_y$ and $n^{\text{HF}} = n_s^{\text{HF}} n_m n_y$ denote the total number of spatiotemporal points for each LF and HF output, respectively. Data are then collected across simulations in the tensors $\mathcal{Z}^{\text{LF}} \in \mathbb{R}^{n_s^{\text{LF}} \times n_m \times n_y \times n_x^{\text{LF}}}$ and $\mathcal{Z}^{\text{HF}} \in \mathbb{R}^{n_s^{\text{HF}} \times n_m \times n_y \times n_x^{\text{HF}}}$, where the temporal modes do not change between fidelities.

3.2.1 Interpolated Low-Fidelity

In the MF framework, we first fit a LF emulator η^{LF} using only the LF ensemble \mathcal{Z}^{LF} following the single-fidelity approach in Section 3.1. To enable coupling with the HF model, each LF basis tensor $\mathcal{B}_{j_s, j_m, j_y}$ is interpolated to the HF mesh by averaging outputs at the k nearest LF grid points, yielding the interpolated basis $\tilde{\mathcal{B}}_{j_s, j_m, j_y} \in \mathbb{R}^{n_s^{\text{HF}} \times n_m \times n_y}$. The resulting interpolated LF emulator is

$$\tilde{\eta}^{\text{LF}}(\mathbf{x}) = \sum_{j_s=1}^{r_s} \sum_{j_m=1}^{r_m} \sum_{j_y=1}^{r_y} \tilde{\mathcal{B}}_{j_s, j_m, j_y} w_{j_s, j_m, j_y}(\mathbf{x}).$$

Fitting the LF emulator yields effective weights $\hat{\gamma}^{\text{LF}}$ evaluated at the LF design set \mathcal{X}^{LF} . If $\mathcal{X}^{\text{HF}} \subset \mathcal{X}^{\text{LF}}$, the HF effective weights $\hat{\gamma}^{\text{HF}}$ are obtained by restricting $\hat{\gamma}^{\text{LF}}$ to the HF design set; otherwise, for $\mathbf{x}^* \in \mathcal{X}^{\text{HF}} \setminus \mathcal{X}^{\text{LF}}$, they are obtained via posterior prediction, using the conditional mean $\mathbb{E}[\gamma^{\text{LF}}(\mathbf{x}^*) \mid \hat{\gamma}^{\text{LF}}]$ as described in Section 3.1.3. As in (3), the observed full weights and the effective weights are related by $\hat{\mathbf{w}}^{\text{HF}} = \tilde{T} \hat{\gamma}^{\text{HF}}$, where $\tilde{T} = G_{(4)}^\top \otimes I_{n_x^{\text{HF}}}$.

3.2.2 Additive Discrepancy Model

Following the additive discrepancy model of Kennedy and O’Hagan (2000), we correct for differences between the LF and HF simulators by representing the HF output as a sum of the interpolated LF emulator, a discrepancy term, and an approximation error,

$$\eta^{\text{HF}}(\mathbf{x}) = \tilde{\eta}^{\text{LF}}(\mathbf{x}) + \delta(\mathbf{x}) + \mathcal{E}_\delta,$$

where $\text{vec}(\mathcal{E}_\delta) \sim \mathcal{N}(\mathbf{0}, \lambda_\delta^{-1} I)$. The discrepancy term $\delta(\mathbf{x}) \in \mathbb{R}^{n_s^{\text{HF}} \times n_m \times n_y}$ captures systematic, input-dependent differences that can vary across the input space and exhibit structured spatiotemporal dependence.

We model the discrepancy using a separate tensor basis representation, constructed analogously to the single-fidelity emulator. We set $\eta^{\text{HF}}(\mathbf{x}) = M^{\text{HF}}(\mathbf{x})$ at the HF design set and compute the HF–LF differences, $\delta(\mathbf{x}) = \eta^{\text{HF}}(\mathbf{x}) - \tilde{\eta}^{\text{LF}}(\mathbf{x})$, for all $\mathbf{x} \in \mathcal{X}^{\text{HF}}$. These discrepancies are stacked in an $n_s^{\text{HF}} \times n_m \times n_y \times n_x^{\text{HF}}$ tensor, to which we apply a Tucker decomposition with ranks (r'_s, r'_m, r'_y, r'_x) , yielding a core tensor \mathcal{G}' and factor matrices U'_s, U'_m, U'_y, U'_x . These components produce the discrepancy bases $\mathcal{D}_{j'_s, j'_m, j'_y}$ and the input-dependent weights $v_{j'_s, j'_m, j'_y}(\mathbf{x})$, following the same basis–weight construction in (2),

$$\delta(\mathbf{x}) = \sum_{j'_s=1}^{r'_s} \sum_{j'_m=1}^{r'_m} \sum_{j'_y=1}^{r'_y} \mathcal{D}_{j'_s, j'_m, j'_y} v_{j'_s, j'_m, j'_y}(\mathbf{x}).$$

Let $\hat{\mathbf{v}}$ be the observed full weights which are directly obtained from the Tucker decomposition above; then, we can obtain effective discrepancy weights $\hat{\zeta}$ similar to (3) which are related by $\hat{\mathbf{v}} = T' \hat{\zeta}$,

where $T' = G'_{(4)} \otimes I_{n_x^{\text{HF}}}$. As with U_x , independent GP priors are placed on each column of U'_x , yielding block-diagonal covariance $\Sigma_\zeta(\mathcal{X}^{\text{HF}}, \mathcal{X}^{\text{HF}})$. The likelihood of the HF data $\mathbf{z}^{\text{HF}} = \text{vec}(\mathcal{Z}^{\text{HF}})$ is then

$$\mathbf{z}^{\text{HF}} \mid \boldsymbol{\gamma}^{\text{HF}}, \boldsymbol{\zeta}, \lambda_\delta \sim \mathcal{N}\left(\tilde{B}\tilde{T}\boldsymbol{\gamma}^{\text{HF}} + DT'\boldsymbol{\zeta}, \lambda_\delta^{-1}I\right)$$

where $\tilde{B} = [I_{n_x^{\text{HF}}} \otimes \tilde{\mathbf{b}}_{111}, \dots, I_{n_x^{\text{HF}}} \otimes \tilde{\mathbf{b}}_{r_s r_m r_y}]$ and $D = [I_{n_x^{\text{HF}}} \otimes \mathbf{d}_{111}, \dots, I_{n_x^{\text{HF}}} \otimes \mathbf{d}_{r'_s r'_m r'_y}]$ are constructed from vectorized bases $\tilde{\mathbf{b}}_{j_s j_m j_y} = \text{vec}(\tilde{\mathcal{B}}_{j_s j_m j_y})$ and $\mathbf{d}_{j'_s j'_m j'_y} = \text{vec}(\mathcal{D}_{j'_s j'_m j'_y})$, respectively. In addition, $\boldsymbol{\gamma}^{\text{HF}}$ and $\boldsymbol{\zeta}$ are the latent effective weights corresponding to the bases $\tilde{\mathbf{b}}$ and \mathbf{d} , respectively.

3.2.3 Multi-Fidelity Posterior Inference

With the proposed MF model, we utilize both LF and HF data in a single model that can be estimated simultaneously across fidelities in a coherent Bayesian model. For notational convenience, let $\boldsymbol{\theta} = [\boldsymbol{\gamma}^{\text{LF}}, \boldsymbol{\gamma}^{\text{HF}}, \boldsymbol{\zeta}]^\top$ be the collection of latent effective weights and $\hat{\boldsymbol{\theta}} = [\hat{\boldsymbol{\gamma}}^{\text{LF}}, \hat{\boldsymbol{\gamma}}^{\text{HF}}, \hat{\boldsymbol{\zeta}}]^\top$ be the collection of all observed effective weights. The joint hierarchical model is

$$\begin{aligned} \begin{bmatrix} \mathbf{z}^{\text{LF}} \\ \mathbf{z}^{\text{HF}} \end{bmatrix} \mid \boldsymbol{\theta}, \lambda_\eta, \lambda_\delta &\sim \mathcal{N}\left(\begin{bmatrix} BT\boldsymbol{\gamma}^{\text{LF}} \\ \tilde{B}\tilde{T}\boldsymbol{\gamma}^{\text{HF}} + DT'\boldsymbol{\zeta} \end{bmatrix}, \begin{bmatrix} \lambda_\eta^{-1}I & \mathbf{0} \\ \mathbf{0} & \lambda_\delta^{-1}I \end{bmatrix}\right) \\ \boldsymbol{\theta} &\sim \mathcal{N}(\mathbf{0}, \Sigma_\theta) \\ \lambda_\eta &\sim \Gamma(a_\eta, b_\eta), \quad \lambda_\delta \sim \Gamma(a_\delta, b_\delta), \end{aligned} \tag{6}$$

where

$$\Sigma_\theta = \begin{bmatrix} \Sigma_\gamma(\mathcal{X}^{\text{LF}}, \mathcal{X}^{\text{LF}}) & \Sigma_\gamma(\mathcal{X}^{\text{LF}}, \mathcal{X}^{\text{HF}}) & \mathbf{0} \\ \Sigma_\gamma(\mathcal{X}^{\text{HF}}, \mathcal{X}^{\text{LF}}) & \Sigma_\gamma(\mathcal{X}^{\text{HF}}, \mathcal{X}^{\text{HF}}) & \mathbf{0} \\ \mathbf{0} & \mathbf{0} & \Sigma_\zeta(\mathcal{X}^{\text{HF}}, \mathcal{X}^{\text{HF}}) \end{bmatrix}.$$

Following an approach analogous to the reduction in Section 3.1.2, we derive a low-dimensional likelihood on the effective weights by reducing the high-dimensional likelihood in (6) without loss of information,

$$\begin{aligned} \hat{\boldsymbol{\theta}} \mid \lambda_\eta, \lambda_\delta &\sim \mathcal{N}(\mathbf{0}, \Sigma_{\hat{\theta}}) \\ \lambda_\eta &\sim \Gamma(a'_\eta, b'_\eta), \quad \lambda_\delta \sim \Gamma(a'_\delta, b'_\delta), \end{aligned} \tag{7}$$

where $\Sigma_{\hat{\theta}} = \Sigma_\theta + \text{blockDiag}[\lambda_\eta^{-1}(C^\top C)^{-1}, \lambda_\delta^{-1}(K^\top K)^{-1}]$ and $K = [\tilde{B}\tilde{T} \quad DT']$. The precision hyperparameters are updated via

$$\begin{aligned} a'_\eta &= a_\eta + \frac{n_x^{\text{LF}}(n_x^{\text{LF}} - r_x)}{2}, & b'_\eta &= b_\eta + \frac{1}{2}(\mathbf{z}^{\text{LF}})^\top \left(I - C(C^\top C)^{-1}C^\top\right) \mathbf{z}^{\text{LF}}, \\ a'_\delta &= a_\delta + \frac{n_x^{\text{HF}}[n_x^{\text{HF}} - (r_x + r'_x)]}{2}, & b'_\delta &= b_\delta + \frac{1}{2}(\mathbf{z}^{\text{HF}})^\top \left(I - K(K^\top K)^{-1}K^\top\right) \mathbf{z}^{\text{HF}}. \end{aligned}$$

See Supplementary Material S1.2 for a detailed derivation. We sample from the posterior of (7) by MCMC with MH updates and hyperpriors similar to those outlined in Section 3.1.2.

Restricting emulation to the effective weights yields a posterior that can be sampled more efficiently than that of a model without dimension reduction. Inverting the covariance $\Sigma_{\hat{\theta}}$ scales as $\mathcal{O}[(n_x^{\text{LF}} r_x + n_x^{\text{HF}}(r_x + r'_x))^3]$, which is substantially cheaper than evaluating the likelihood in the unreduced setting, $\mathcal{O}[(n_x^{\text{LF}} n_x^{\text{LF}} + n_x^{\text{HF}} n_x^{\text{HF}})^3]$.

3.2.4 Multi-Fidelity Posterior Prediction

Unlike single-fidelity emulators, MF emulators integrate information from both LF and HF data, enhancing prediction accuracy and capturing the uncertainties in each fidelity as well as their discrepancies. As in Section 3.1.3, we derive the posterior predictive distribution of for an untested \mathbf{x}^* via the conditional properties of multivariate normal distributions on the joint

$$\begin{bmatrix} \hat{\gamma}^{\text{LF}} \\ \hat{\gamma}^{\text{HF}} \\ \hat{\zeta} \\ \gamma^* \\ \zeta^* \end{bmatrix} \Big| \lambda_\eta, \lambda_\delta \sim \mathcal{N} \left(\mathbf{0}, \begin{array}{ccc|cc} & & \Sigma_{\hat{\theta}} & & \\ & & & \Sigma_\gamma(\mathcal{X}^{\text{LF}}, \mathbf{x}^*) & \mathbf{0} \\ & & & \Sigma_\gamma(\mathcal{X}^{\text{HF}}, \mathbf{x}^*) & \mathbf{0} \\ & & & \mathbf{0} & \Sigma_\zeta(\mathcal{X}^{\text{HF}}, \mathbf{x}^*) \\ \hline \Sigma_\gamma(\mathbf{x}^*, \mathcal{X}^{\text{LF}}) & \Sigma_\gamma(\mathbf{x}^*, \mathcal{X}^{\text{HF}}) & \mathbf{0} & \Sigma_\gamma(\mathbf{x}^*, \mathbf{x}^*) & \mathbf{0} \\ \mathbf{0} & \mathbf{0} & \Sigma_\zeta(\mathbf{x}^*, \mathcal{X}^{\text{HF}}) & \mathbf{0} & \Sigma_\zeta(\mathbf{x}^*, \mathbf{x}^*) \end{array} \right).$$

For each posterior predictive draw of (γ^*, ζ^*) , we obtain a spatiotemporal prediction

$$\eta^{\text{HF}}(\mathbf{x}^*) \mid \mathcal{Z}_1, \mathcal{Z}_2 = \tilde{B}_\eta G_{(4)}^\top \gamma^* + D_\delta G_{(4)}^\top \zeta^* + \epsilon_\delta,$$

where $\tilde{B}_\eta = [\tilde{\mathbf{b}}_{111}, \dots, \tilde{\mathbf{b}}_{r_s r_m r_y}]$ and $D_\delta = [\mathbf{d}_{111}, \dots, \mathbf{d}_{r'_s r'_m r'_y}]$.

4 Simulation Study

We tested our method on synthetic data generated from functions with known analytical forms, allowing direct and efficient comparison of emulator predictions to true simulator outputs. The deterministic simulator, adapted from Shubert function (Surjanovic and Bingham, 2013), maps input $\mathbf{x} = [x_1, x_2, x_3]^\top \in [0, 1]^3$ to spatiotemporal fields over spatial coordinates $\mathbf{s} = (s_1, s_2)$, months m , and years $y = 1, \dots, 5$. A second deterministic function was used to generate an additive discrepancy term, which was combined to the first simulator to produce the final HF outputs. Simulations were conducted on 25×25 and 50×50 grids for the LF and HF configurations, respectively. We generated a Latin hypercube sample of size $n_x^{\text{LF}} = 100$ for LF design points and selected a subset of $n_x^{\text{HF}} = 10$ for HF design points.

The simulation study design followed two principles: first, inducing a significant LF–HF discrepancy so that the LF simulator, even after interpolation, cannot reliably predict unobserved HF outputs; and second, ensuring adequate input-space variability in the HF response so that the sparsely sampled HF data alone are insufficient to recover the full model behavior. Additionally, we created x_3 as a dummy variable that does not affect either the LF or HF outputs. This design allows us to evaluate the robustness of the proposed emulator to irrelevant input dimensions. Complete functional forms and additional simulation details are provided in the Code and Data reference in the Supplementary Materials.

We compared four emulation approaches: (1) LF-Tensor, a single-fidelity tensor emulator trained on LF data and interpolated to the fine grid; (2) HF-Tensor, a single-fidelity tensor emulator trained on HF data; (3) MF-Tensor, a multi-fidelity tensor emulator combining LF and HF data; and (4) Naïve-GP, a baseline Gaussian process emulator fit independently at each spatial location and time of the HF data. The LF-Tensor and HF-Tensor emulators follow the single-fidelity method outlined in Section 3.1, while the MF-Tensor emulator follows the approach outlined in Section 3.2.

Emulator predictions were evaluated at 100 random test inputs \mathbf{x}^* using three metrics: mean squared error (MSE) computed against the HF output, posterior standard deviation (SD), and 95% credible interval coverage. To compute MSE, we evaluated the simulator at the unobserved test inputs, which was feasible in this experiment because the simulator runs quickly. For SD

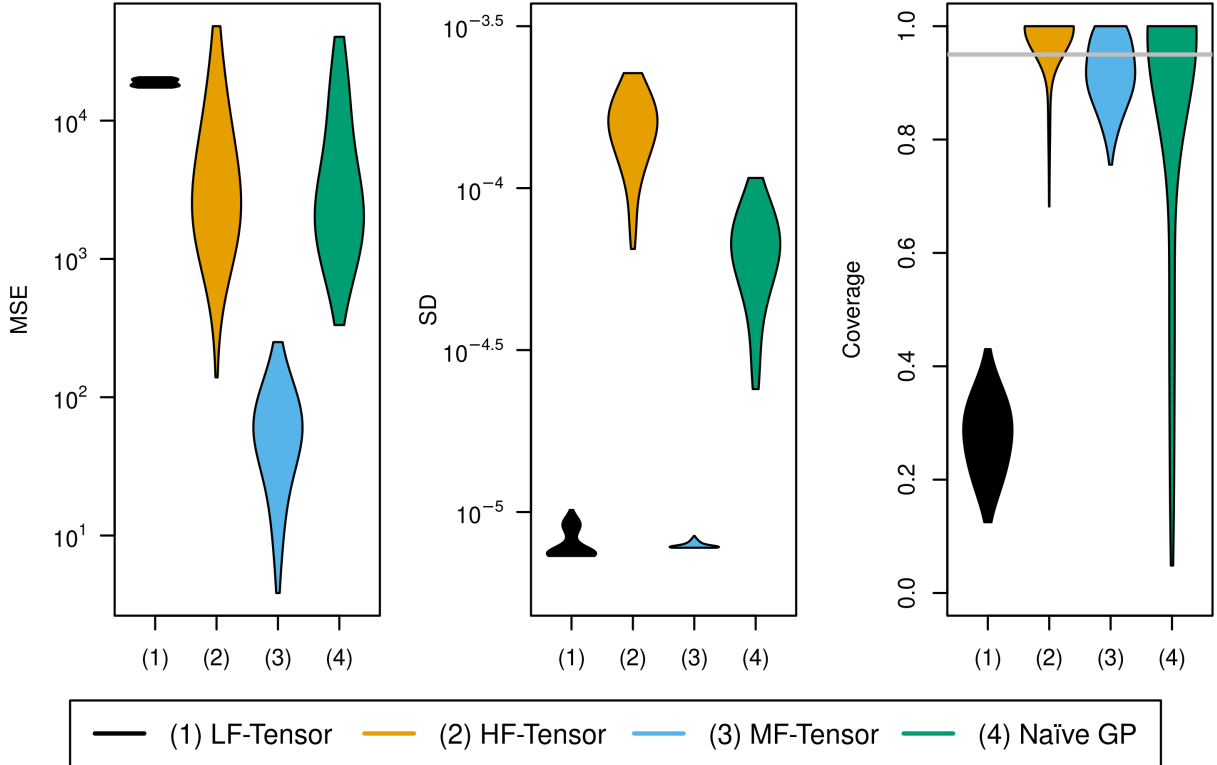


Figure 3: Results from the simulation study. Violin plots comparing MSE, SD, and 95% credible interval (gray line indicates target) coverage for four emulators: tensor emulators trained on low-fidelity (LF) and high-fidelity (HF) data, a multi-fidelity (MF) tensor emulator, and a baseline Gaussian process emulator fit independently at each spatial and temporal location (Naïve-GP). Metrics are averaged over spatial location and time.

comparisons, we normalized the posterior predictive standard deviations by each emulator’s output range to obtain dimensionless uncertainty measures, enabling meaningful comparison across fidelities despite differing output scales.

Tensor-based methods selected mode-specific ranks to capture 99% of the explained variance, resulting in $(r_s, r_m, r_y, r_x) = (4, 3, 2, 4)$ for the LF and HF tensors, and $(r'_s, r'_m, r'_y, r'_x) = (3, 3, 1, 4)$ for the discrepancy tensor. Three MCMC chains of 4,000 iterations with a burn-in length of 2,000 were used. Additional details about our MCMC implementation and diagnostic procedures can be found in Supplementary Material B.

Figure 3 illustrates the performance of the four emulators averaged over spatial location and time. The LF-Tensor has low SD but high MSE and poor coverage due to ignoring fidelity discrepancies, while the HF-Tensor improves upon MSE but suffers from inflated SD because of limited training data. The Naïve-GP has similar MSE and slightly better SD compared to the HF-Tensor, but lacks inference into spatiotemporal dynamics and yields poorly calibrated coverage. In contrast, the MF-Tensor emulator outperforms all others by effectively using both low- and high-resolution data, achieving the lowest MSE, SD comparable to the LF-Tensor, and coverage near the target level of 0.95.

Beyond predictive performance and uncertainty quantification, our approach also provides esti-

Table 1: Posterior mean length scales of the low-fidelity (LF) and discrepancy terms for each effective weight (EW) and input in the MF-Tensor emulator from the simulation study. The LF and discrepancy components come from Tucker decompositions of the simulated data with ranks $r_x = 4$ and $r'_x = 4$. Large length scales indicate inputs with little effect on the output; in particular, the MF emulator identifies outputs as generally less sensitive to x_3 .

	Low-Fidelity				Discrepancy			
	EW1	EW2	EW3	EW4	EW1	EW2	EW3	EW4
x_1	0.18	0.26	0.19	0.19	4.03	0.49	1.25	0.44
x_2	0.34	0.11	0.13	0.24	0.98	1.02	0.17	0.40
x_3	2.46	2.90	3.12	1.72	6.33	1.38	1.50	1.92

mates of input parameter sensitivity. Table 1 summarizes the MCMC mean length scales for each input–weight combination from the MF-Tensor emulator. Length scales indicate how sensitive the model output is to changes in each input, with smaller values corresponding to higher sensitivity. As expected, the dummy input x_3 has no effect on either the LF or discrepancy functions, and the MF-Tensor emulator correctly assigns it consistently large length scales. In contrast, x_1 and x_2 generally have smaller length scales.

5 MPAS-Seaice Emulation

We evaluated model performance with a validation study using the MPAS-Seaice data. For each of the $n_x^{\text{HF}} = 21$ inputs with both LF and HF runs, we conducted leave-one-out cross-validation (LOO-CV), training separate LF, HF, MF, and Naïve-GP emulators as in Section 4, and making predictions for the output from the held-out design point. Performance was evaluated using the same metrics (MSE, SD, and 95% coverage) and MCMC settings described in Section 4.

We determined the Tucker ranks for both the LF and HF tensors by retaining 99% of the variance in each decomposition, and then selected the final ranks as the maximum across the two sets. This resulted in $(r_s, r_m, r_y, r_x) = (79, 7, 6, 4)$. For the discrepancy, we targeted 80% explained variance, yielding $(r'_s, r'_m, r'_y, r'_x) = (82, 7, 7, 4)$; a higher target (e.g., 99%) would have required hundreds of spatial bases. Compared to the previous simulation study, MPAS-Seaice exhibits more spatial variability, requiring a larger number of bases. The Tucker decomposition naturally supports this mode-specific flexibility, enabling efficient dimensionality reduction even when variability differs substantially across modes.

Tucker decomposition produced spatial, monthly, and yearly bases (i.e., the columns of factor matrices) whose importance was quantified via squared entries of the core tensor, normalized by its total variance (Sidiropoulos et al., 2017). Figure 4 shows the first three bases for the spatial, monthly, and yearly modes in the Tucker decomposition of the LF data. The leading spatial basis represents typical ice transitions in colder months, whereas the second and third capture transitions more common in warmer months. The first two monthly bases describe the seasonal cycle, and the first two yearly bases highlight a general decline in sea ice from 1999 through 2009. The third temporal bases indicate more irregular patterns, capturing fine-scale variation. In each mode, the first basis explains over 90% of the relative variance.

Figure 5 compares the monthly and yearly performance of the emulators. Seasonal patterns are evident across all emulators, with increased MSE and SD from June through September, but

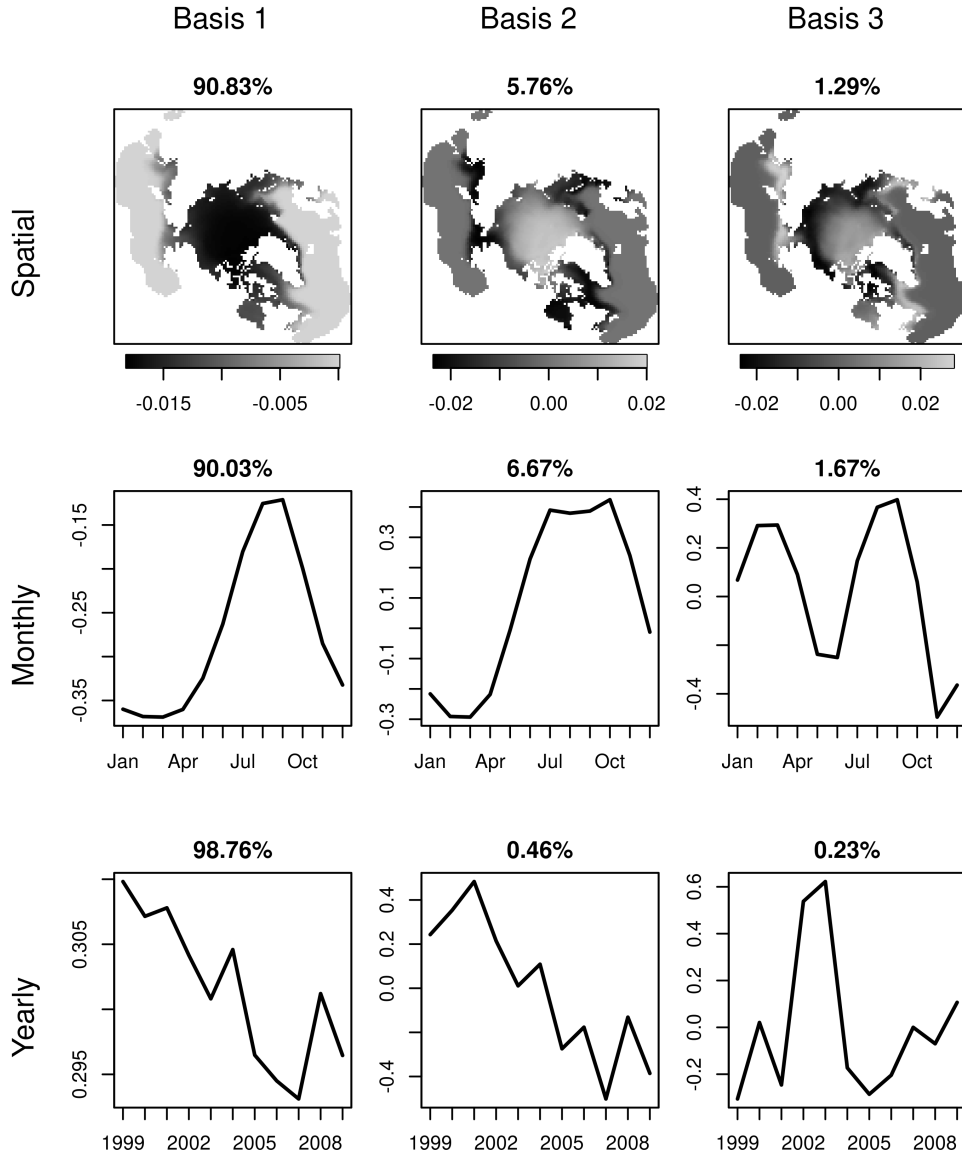


Figure 4: First three spatial, monthly, and yearly bases from the Tucker decomposition of low-fidelity MPAS-Seaice data. Spatial bases capture typical ice transitions, monthly bases reflect the seasonal cycle, and yearly bases show long-term decline in sea ice extent. Relative contributions are shown as percentages of total variance for each mode, with the leading basis in every mode explaining over 90% of the variance.

Table 2: Posterior mean length scales of the LF and discrepancy terms for each effective weight (EW) and input variable in the MF-Tensor emulator applied to MPAS-Seaice data. The 6 input parameters consist of snow conductivity (`ksno`), ocean-ice drag (`dragio`), melt pond drainage (`lambda_pond`), two parameters controlling snow grain size (`rsnw_mlt`, `R_snw`), and solid fraction at the ice-ocean interface (`phi_i_mushy`).

	Low-Fidelity				Discrepancy			
	EW1	EW2	EW3	EW4	EW1	EW2	EW3	EW4
<code>ksno</code>	1.22	0.47	0.32	0.39	2.26	0.32	0.97	0.34
<code>dragio</code>	4.12	1.40	0.54	1.28	4.52	6.03	1.06	2.48
<code>lambda_pond</code>	7.47	1.21	2.74	1.59	5.18	1.57	8.11	4.17
<code>rsnw_mlt</code>	6.98	2.35	6.94	0.92	4.19	1.83	5.29	2.24
<code>R_snw</code>	1.98	1.89	4.95	1.48	12.68	2.01	3.47	1.99
<code>phi_i_mushy</code>	61.31	7.09	2.93	5.83	6.63	5.06	3.63	8.76

no clear trends across years. Overall, the MF-Tensor emulator outperforms both the LF- and HF-Tensor emulators in MSE and standard deviation, while matching HF in coverage. The LF-Tensor exhibits lower MSE than the HF-Tensor during the warmer months in the LOO-CV study because the limited number of HF runs means that, when an outlying summer trend is left out of training, the HF-Tensor struggles to predict that held-out case, resulting in elevated MSE.

In warmer months, when variability is higher, the Naïve-GP performs worse than the MF-Tensor in terms of MSE and SD. Its per-location GPs ignore spatiotemporal dependence, which reduces accuracy and inflates uncertainty. In cold months, the Naïve-GP shows lower MSE and SD than the MF-Tensor, but this apparent advantage arises because many locations are constant across inputs (all ice or no ice), causing the GP to degenerate. At these locations, errors and uncertainty are effectively forced to zero and coverage to one. Thus, the Naïve-GP’s better performance in cold months reflects degeneracy rather than genuinely superior modeling.

Figure 6 shows spatial patterns of MSE and SD. Sea ice variability is highest along thin transitional boundaries in cold months and across the Central Arctic in warm months. To illustrate these differences, we focus on March and September. By leveraging both LF and HF data, the MF-Tensor emulator reduces MSE and SD in regions of high variability. The Naïve-GP emulator has poorly calibrated uncertainty, with large SD in regions of high variability.

The average posterior length scales for each input variable and effective weight in the MF-Tensor emulator, computed using the full data rather than LOO-CV, are reported in Table 2. Across all effective weights, thermal conductivity of snow (`ksno`) consistently exhibits the smallest length scales in both the LF and discrepancy components, indicating that MPAS-Seaice is most sensitive to this parameter. In contrast, solid fraction at the ice-ocean interface (`phi_i_mushy`) shows substantially larger length scales, meaning the response varies only weakly with respect to that variable. Length scales differ between effective weights, reflecting that each effective weight captures a distinct combination of input-driven variability.

The LF-Tensor emulator completed a LOO-CV in 52.4 minutes, whereas the HF-Tensor emulator required 83.4 minutes. The MF-Tensor was slower at 175.5 minutes per LOO-CV because of its greater complexity, specifically the expanded training dataset and larger number of GP hyperparameters. Nonetheless, the MF-Tensor remained a feasible option as it is more efficient than performing all MPAS-Seaice runs at high-resolution (see Figure 1).

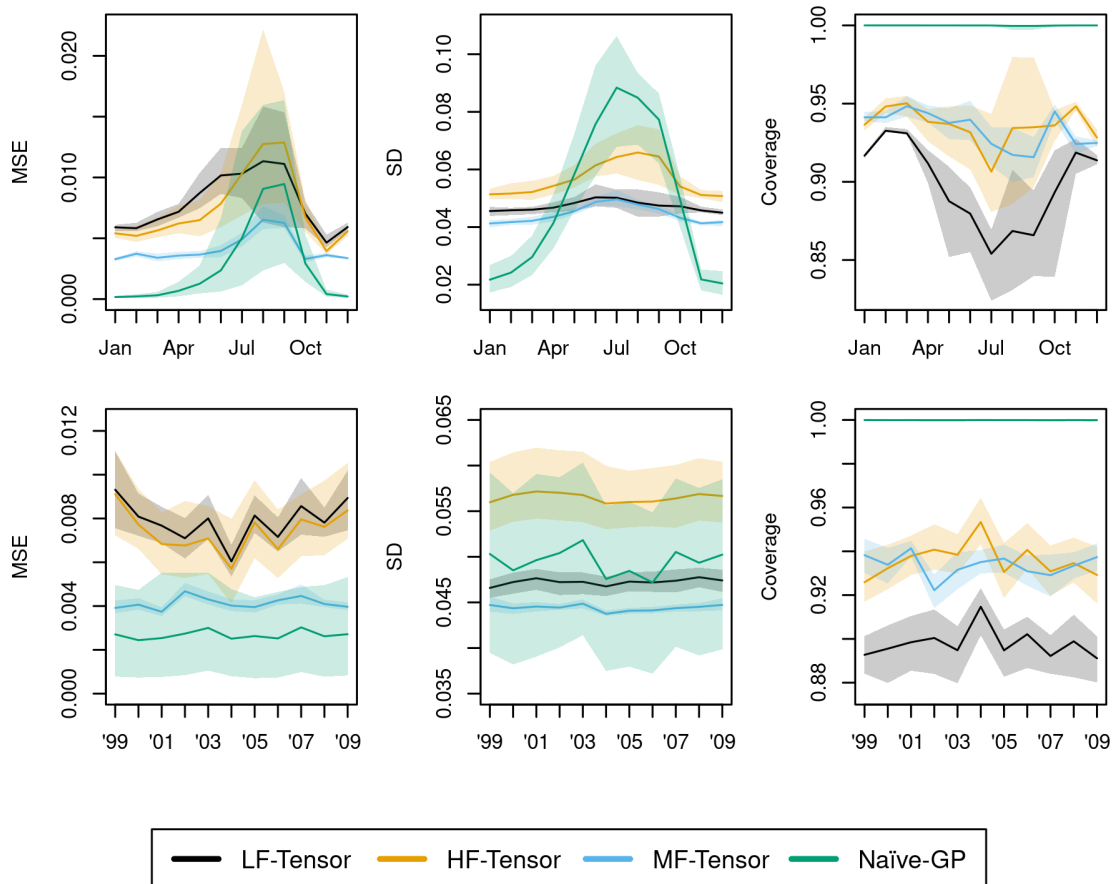


Figure 5: Monthly and yearly performance of emulators on MPAS-Seaice data. Mean across LOO-CV with 2.5%–95.5% LOO-CV quantile bands. Seasonal patterns are evident, with increased bias and uncertainty from June through September reflecting greater variability in MPAS-Seaice outputs during those months. The Naïve-GP shows lower MSE and SD in colder months only because, at many spatiotemporal locations, the outputs are constant across all inputs (all ice or no ice); in warmer months, its per-location GPs fail to capture spatiotemporal dependencies, leading to reduced accuracy and inflated uncertainty.

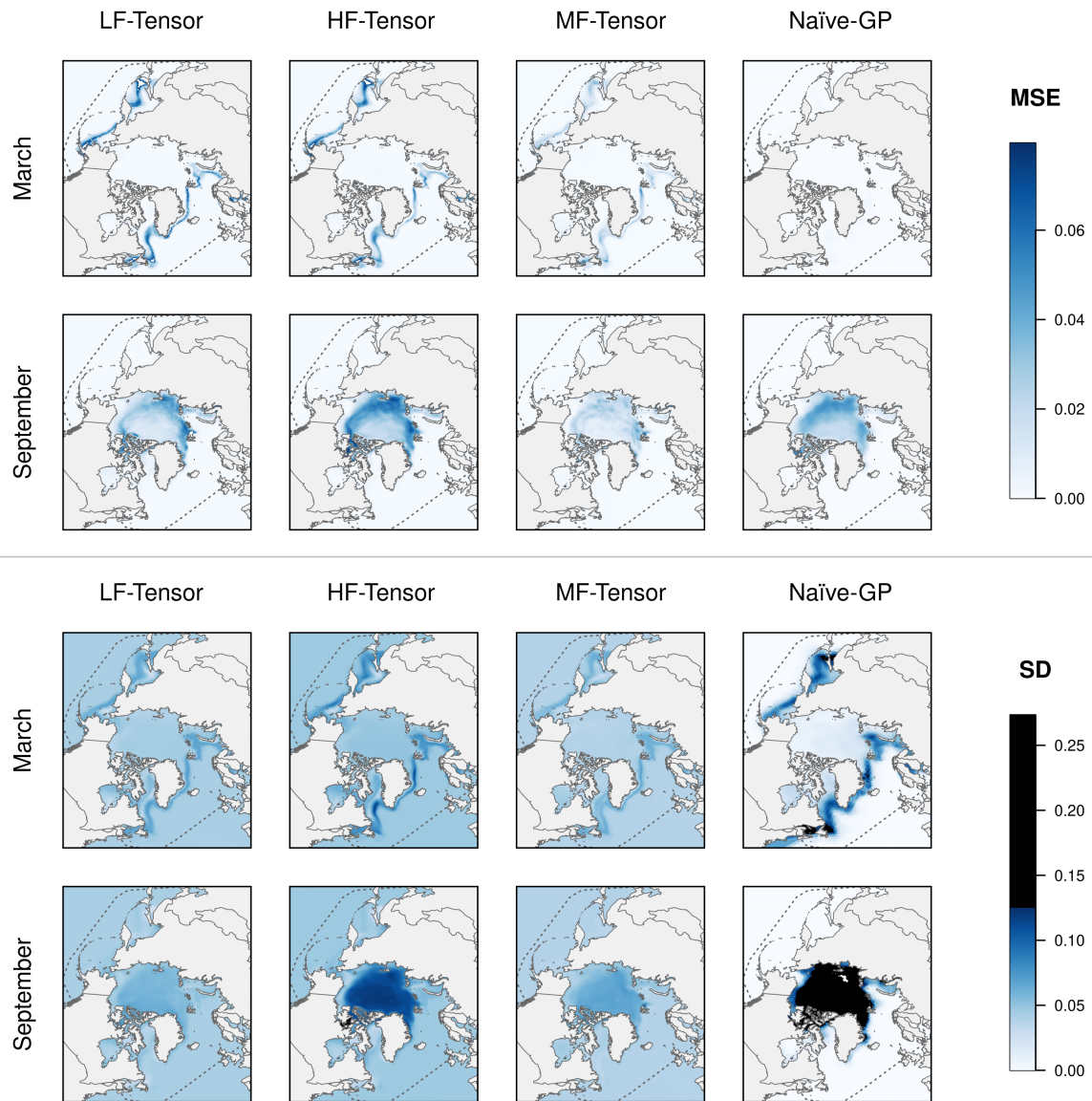


Figure 6: Spatial performance comparison of emulators on MPAS-Seaice data, showing mean squared error (MSE) in the top panels and standard deviation (SD) in the bottom panels, each averaged over leave-one-out cross validation and time at each spatial location. The MPAS-Seaice domain is outlined with a dotted line, and SD values are truncated at 0.125 for clear visual comparison. March displays higher variability in thin transitional ice bands, while September shows elevated variability across the Central Arctic and surrounding seas. In these high-variability regions, the MF-Tensor emulator generally attains the lowest MSE and SD, roughly matching the performance of other emulators at times.

6 Discussion

We propose a multi-fidelity (MF) tensor emulation framework for large-scale earth system models that combines the computational efficiency of low-fidelity (LF) simulations with the accuracy of high-fidelity (HF) simulations. Using Tucker decomposition for dimension reduction, the method captures the high-dimensional, spatiotemporal structure of sea-ice processes in MPAS-Seaice, providing a compact representation that enables both accurate emulation and interpretation of the physical drivers of variability. Through a simulation study with synthetic data and a validation study with MPAS-Seaice, we show that the MF-Tensor emulator consistently outperforms single-fidelity and naïve per-location Gaussian process emulators in predictive accuracy and uncertainty quantification, achieving lower MSE and posterior uncertainty in regions of high spatiotemporal variability, and well-calibrated credible intervals. These results demonstrate the value of multi-fidelity, tensor-based emulation for efficiently capturing complex earth system processes.

The MF-Tensor emulator is broadly applicable across a wide range of modeling scenarios, making it a versatile tool for complex MF simulations. While we focused on spatial resolution to distinguish fidelities, the method generalizes to other hierarchies such as differences in numerical resolution (Harvey and Verseghy, 2016) or the underlying complexity of simulation physics (Maher and Gerber, 2019), and can be extended to more than two fidelities (Kennedy and O’Hagan, 2000). By including a nugget in the GPs, our method can also handle noisy, non-deterministic simulations (Gramacy, 2020). Furthermore, our approach does not require nested input designs or spatiotemporal grids across fidelities, enabling it to accommodate realistic workflows where simulations differ in resolution, domain, or parameterization (Perron et al., 2022; Gruber et al., 2023; Waling et al., 2024). The MF-Tensor emulator can also be integrated into adaptive experimental design strategies, leveraging its fast, uncertainty-aware predictions to efficiently determine both where to sample next and which fidelity level to use (Song et al., 2019; Pellegrini et al., 2023; Garbo et al., 2024).

While our analysis focused on fourth-order tensors (spatial location, month, year, and design input), the MF-Tensor framework generalizes to tensors of arbitrary size. For example, we considered modeling the MPAS-Seaice data with a third-order tensor by combining year and month into a single temporal mode. However, this approach resulted in predictions that were less accurate and more uncertain (see Supplementary Figure S3). Collapsing the temporal dimensions prevented the model from exploiting the low-rank structure arising from repeated seasonal patterns across years, thereby reducing the effectiveness of dimension reduction and degrading emulation performance.

Several promising directions exist for extending the MF-Tensor framework beyond its current formulation. At present, each effective weight is modeled independently as a GP, justified by the orthogonality of the columns of U_x , but this assumption may be restrictive when weights exhibit nonlinear dependencies or non-Gaussian behavior. Deep GPs (Damianou and Lawrence, 2013) and neural-network-based surrogates (Wu et al., 2022; Niu et al., 2024) offer greater expressivity, though neural networks often require higher data requirements and limited uncertainty quantification. In addition, Bayesian triangular transport maps provide a principled alternative for capturing nonlinear dependence structures (Katzfuss and Schäfer, 2023; Calle-Saldarriaga et al., 2025).

Complementary advances in tensor decomposition could further enhance flexibility and scalability, including methods that allow more general spatial or temporal arrangements within a fidelity (Tang et al., 2025), functional tensor decompositions for extrapolation to new spatiotemporal locations (Han et al., 2023), and generalized CP decompositions that employ non- ℓ_2 loss functions to improve robustness to outliers and non-Gaussian residuals (Hong et al., 2020). Together, these extensions point to a rich set of opportunities for improving the expressivity and applicability of MF tensor emulation in realistic simulation settings.

By fusing information across fidelities, our MF method enables practitioners to make effective

use of limited high-resolution simulations by systematically leveraging cheaper, lower-resolution runs. This capability is increasingly important as earth system models grow in complexity and computational cost, constraining the number of scenarios that can be explored (Schneider et al., 2017). The MF-Tensor emulator provides a practical pathway for tasks such as calibration, and scenario exploration, and sensitivity analysis that would otherwise perform worse using LF or HF data alone. Its flexibility and computational efficiency make it well suited for integration into real-world modeling workflows in earth system science (Gruber et al., 2023; Jakeman et al., 2025), engineering design (Desai et al., 2023; He and Luo, 2024), and other domains where informed decision-making depends on balancing simulation accuracy, cost, and uncertainty (Peherstorfer et al., 2018).

Acknowledgments. E3SM v3.0.2 was obtained from the Energy Exascale Earth System Model project, sponsored by the U.S. Department of Energy, Office of Science, Office of Biological and Environmental Research Earth Systems Model Development Program area of Earth and Environmental System Modeling.

Funding. This material is based upon work supported by the U.S. Department of Energy, Office of Science, Office of Biological and Environmental Research, under Award Number DE-SC0023366.

This research used resources of the National Energy Research Scientific Computing Center (NERSC), a Department of Energy User Facility using NERSC award BER-ERCAP-0032240.

Supplement to “A Multi-Fidelity Tensor Emulator for Spatiotemporal Outputs: Emulation of Arctic Sea Ice Dynamics”. Please contact the corresponding authors for the supplementary material. The supplementary material contains two sections. Supplement S1 provides detailed derivations for the results presented in Section 3. Supplement S2 includes additional figures.

Code and Data. We implemented the proposed methods in R. The code and results for the simulation study, example model runs, and detailed instructions will be available at https://github.com/tjcontant/mf_tensor. Due to the large file size of the full MPAS–Seaice model output, only model runs for a smaller domain are provided in the GitHub repository.

References

- Anima Anandkumar, Prateek Jain, Yang Shi, and U. N. Niranjan. Tensor vs. matrix methods: Robust tensor decomposition under block sparse perturbations. In Arthur Gretton and Christian C. Robert, editors, *Proceedings of the 19th International Conference on Artificial Intelligence and Statistics*, volume 51 of *Proceedings of Machine Learning Research*, pages 268–276, Cadiz, Spain, 09–11 May 2016. PMLR.
- Grey Ballard and Tamara G. Kolda. *Tensor Decompositions for Data Science*. Cambridge University Press, 2025.
- Simeon Bird, Martin Fernandez, Ming-Feng Ho, Mahdi Qezlou, Reza Monadi, Yueying Ni, Nianyi Chen, Rupert Croft, and Tiziana Di Matteo. Priya: A new suite of lyman- α forest simulations for cosmology. *Journal of Cosmology and Astroparticle Physics*, 2023(10), October 2023. ISSN 1475-7516.
- Ed Blockley, Martin Vancoppenolle, Elizabeth Hunke, Cecilia Bitz, Daniel Feltham, Jean-François

- Lemieux, Martin Losch, Eric Maisonnave, Dirk Notz, Pierre Rampal, Steffen Tietsche, Bruno Tremblay, Adrian Turner, François Massonnet, Einar Ólason, Andrew Roberts, Yevgeny Aksenov, Thierry Fichet, Gilles Garric, Doroteaciro Iovino, Gurvan Madec, Clément Rousset, David Salas y Melia, and David Schroeder. The future of sea ice modeling: Where do we go from here? *Bulletin of the American Meteorological Society*, 101(8):E1304 – E1311, 2020.
- Veronica E. Bowman and David C. Woods. Emulation of multivariate simulators using thin-plate splines with application to atmospheric dispersion. *SIAM/ASA Journal on Uncertainty Quantification*, 4(1):1323–1344, 2016.
- B. P. Briegleb and B. Light. A Delta-Eddington multiple scattering parameterization for solar radiation in the sea ice component of the Community Climate System Model. Technical Report NCAR/TN-472+STR, National Center for Atmospheric Research, Boulder, Colorado USA., 2007.
- Alejandro Calle-Saldarriaga, Paul F. V. Wiemann, and Matthias Katzfuss. Generative multi-fidelity modeling and downscaling via spatial autoregressive transport maps. <https://arxiv.org/abs/2509.22474>, 2025.
- D. Chen, M. Rojas, B.H. Samset, K. Cobb, A. Diongue Niang, P. Edwards, S. Emori, S.H. Faria, E. Hawkins, P. Hope, P. Huybrechts, M. Meinshausen, S.K. Mustafa, G.-K. Plattner, and A.-M. Tréguier. *Framing, Context, and Methods*, page 147–286. Cambridge University Press, Cambridge, United Kingdom and New York, NY, USA, 2021.
- William D. Collins, Cecilia M. Bitz, Maurice L. Blackmon, Gordon B. Bonan, Christopher S. Bretherton, James A. Carton, Ping Chang, Scott C. Doney, James J. Hack, Thomas B. Henderson, Jeffrey T. Kiehl, William G. Large, Daniel S. McKenna, Benjamin D. Santer, and Richard D. Smith. The Community Climate System Model Version 3 (CCSM3). *Journal of Climate*, 19(11): 2122 – 2143, 2006.
- Noel Cressie. *Statistics for Spatial Data*. Wiley, New York, 1993.
- Andreas Damianou and Neil D. Lawrence. Deep Gaussian processes. In Carlos M. Carvalho and Pradeep Ravikumar, editors, *Proceedings of the Sixteenth International Conference on Artificial Intelligence and Statistics*, volume 31 of *Proceedings of Machine Learning Research*, pages 207–215, Scottsdale, Arizona, USA, 29 Apr–01 May 2013. PMLR.
- Lieven De Lathauwer, Bart De Moor, and Joos Vandewalle. On the best rank-1 and rank-(r_1, r_2, \dots, r_n) approximation of higher-order tensors. *SIAM Journal on Matrix Analysis and Applications*, 21(4):1324–1342, 2000.
- Aarya Sheetal Desai, Navaneeth N., Sondipon Adhikari, and Souvik Chakraborty. Enhanced multi-fidelity modeling for digital twin and uncertainty quantification. *Probabilistic Engineering Mechanics*, 74:103525, 2023. ISSN 0266-8920.
- E3SM Project. Energy Exascale Earth System Model (E3SM). [Computer Software], December 2024. URL <https://dx.doi.org/10.11578/E3SM/dc.20241216.1>.
- Ayesha Ekanayaka, Emily L Kang, Amy Braverman, and Peter Kalmus. A multivariate spatial statistical model for statistical downscaling of sea surface temperature in the great barrier reef region. *Journal of the Royal Statistical Society Series C: Applied Statistics*, 74(4):1183–1213, 03 2025. ISSN 0035-9254.

- M. Giselle Fernández-Godino. Review of multi-fidelity models. *Advances in Computational Science and Engineering*, 1(4):351–400, 2023.
- Alexander I.J Forrester, András Sóbester, and Andy J Keane. Multi-fidelity optimization via surrogate modelling. *Proceedings of the Royal Society A: Mathematical, Physical and Engineering Sciences*, 463(2088):3251–3269, 2007.
- Andrea Garbo, Jigar Parekh, Tilo Rischmann, and Philipp Bekemeyer. Multi-fidelity adaptive sampling for surrogate-based optimization and uncertainty quantification. *Aerospace*, 11(6):448, 2024.
- Paolo Giordani and Henk A. L. Kiers. Principal component analysis with boundary constraints. *Journal of Chemometrics*, 21(12):547–556, 2007.
- Robert B. Gramacy. *Surrogates: Gaussian Process Modeling, Design and Optimization for the Applied Sciences*. Chapman Hall/CRC, Boca Raton, Florida, 2020.
- Stephen M. Griffies, Arne Biastoch, Claus Böning, Frank Bryan, Gokhan Danabasoglu, Eric P. Chassignet, Matthew H. England, Rüdiger Gerdes, Helmuth Haak, Robert W. Hallberg, Wilco Hazeleger, Johann Jungclauss, William G. Large, Gervan Madec, Anna Pirani, Bonita L. Samuels, Markus Scheinert, Alex Sen Gupta, Camiel A. Severijns, Harper L. Simmons, Anne Marie Treguier, Mike Winton, Stephen Yeager, and Jianjun Yin. Coordinated Ocean-ice Reference Experiments (COREs). *Ocean Modelling*, 26(1):1–46, 2009.
- A. Gruber, M. Gunzburger, L. Ju, R. Lan, and Z. Wang. Multifidelity monte carlo estimation for efficient uncertainty quantification in climate-related modeling. *Geoscientific Model Development*, 16(4):1213–1229, 2023.
- Rungang Han, Pixu Shi, and Anru R. Zhang. Guaranteed functional tensor singular value decomposition. *Journal of the American Statistical Association*, 119(546):995–1007, 2023.
- R. Harvey and D. L. Verseghy. The reliability of single precision computations in the simulation of deep soil heat diffusion in a land surface model. *Climate Dynamics*, 46(11–12):3865–3882, 2016.
- Simon Haykin. *Neural Networks: A Comprehensive Foundation*. Prentice Hall PTR, USA, 2nd edition, 1998. ISBN 0132733501.
- Youwei He and Jinliang Luo. Efficient hierarchical kriging modeling method for high-dimension multi-fidelity problems. *Chinese Journal of Mechanical Engineering*, 37, 2024.
- Dave Higdon, James Gattiker, Brian Williams, and Maria Rightley. Computer model calibration using high-dimensional output. *Journal of the American Statistical Association*, 103(482):570–583, 2008.
- David Hong, Tamara G. Kolda, and Jed A. Duersch. Generalized canonical polyadic tensor decomposition. *SIAM Review*, 62(1):133–163, 2020.
- Likeng Huang, Zhenghong Gao, and Dehu Zhang. Research on multi-fidelity aerodynamic optimization methods. *Chinese Journal of Aeronautics*, 26(2):279–286, 2013. ISSN 1000-9361.
- E. C. Hunke, W. H. Lipscomb, A. K. Turner, N. Jeffery, and S. Elliott. CICE: the Los Alamos sea ice model documentation and software user’s manual version 5.1. Technical report, Los Alamos National Laboratory, 2015.

- Elizabeth C. Hunke, David A. Hebert, and Olivier Lecomte. Level-ice melt ponds in the Los Alamos sea ice model, CICE. *Ocean Modelling*, 71:26–42, 2013. Arctic Ocean.
- John D. Jakeman, Mauro Perego, D. Thomas Seidl, Tucker A. Hartland, Trevor R. Hillebrand, Matthew J. Hoffman, and Stephen F. Price. An evaluation of multi-fidelity methods for quantifying uncertainty in projections of ice-sheet mass change. *Earth System Dynamics*, 16:513–544, 2025.
- Nicole Jeffery, Mathew E. Maltrud, Elizabeth C. Hunke, Shanlin Wang, Jon Wolfe, Adrian K. Turner, Susannah M. Burrows, Xiaoying Shi, William H. Lipscomb, Wieslaw Maslowski, and et al. Investigating controls on sea ice algal production using E3SMv1.1-BGC. *Annals of Glaciology*, 61(82):51–72, 2020.
- Fujiao Ju, Yanfeng Sun, Junbin Gao, Yongli Hu, and Baocai Yin. Vectorial dimension reduction for tensors based on bayesian inference. *IEEE Transactions on Neural Networks and Learning Systems*, 29(10):4579–4592, 2018.
- Matthias Katzfuss and Florian Schäfer. Scalable bayesian transport maps for high-dimensional non-gaussian spatial fields. *Journal of the American Statistical Association*, 119(546):1409–1423, 2023.
- MC Kennedy and A O’Hagan. Predicting the output from a complex computer code when fast approximations are available. *Biometrika*, 87(1):1–13, 03 2000. ISSN 0006-3444.
- Henk A. L. Kiers and Iven Van Mechelen. Three-way component analysis: Principles and illustrative application. *Psychological Methods*, 6(1):84–110, mar 2001.
- Tamara G. Kolda and Brett W. Bader. Tensor decompositions and applications. *SIAM Review*, 51(3):455–500, 2009.
- Yuki Kosaka, Shinya Kobayashi, Yayoi Harada, Chiaki Kobayashi, Hiroaki Naoe, Koichi Yoshimoto, Masashi Harada, Naochika Goto, Jotaro Chiba, Kengo Miyaoka, Ryohei Sekiguchi, Makoto Deushi, Hirotaka Kamahori, Tosiya Nakaegawa, Taichu Y. Tanaka, Takayuki Tokuhira, Yoshiaki Sato, Yasuhiro Matsushita, and Kazutoshi Onogi. The JRA-3Q Reanalysis. *Journal of the Meteorological Society of Japan. Ser. II*, 102(1):49–109, 2024.
- L. Ruby Leung, David C. Bader, Mark A. Taylor, and Renata B. McCoy. An introduction to the E3SM special collection: Goals, science drivers, development, and analysis. *Journal of Advances in Modeling Earth Systems*, 12(11):e2019MS001821, 2020.
- James Li, Jacob Bien, and Martin T. Wells. rTensor: an R package for multidimensional array (tensor) unfolding, multiplication, and decomposition. *Journal of Statistical Software*, 87(10), 2018.
- William H. Lipscomb and Elizabeth C. Hunke. Modeling sea ice transport using incremental remapping. *Monthly Weather Review*, 132(6):1341 – 1354, 2004.
- William H. Lipscomb, Elizabeth C. Hunke, Wieslaw Maslowski, and Jaromir Jakacki. Ridging, strength, and stability in high-resolution sea ice models. *Journal of Geophysical Research: Oceans*, 112(C3), 2007.
- Xinwang Liu, Weiwen Zhao, and Decheng Wan. Multi-fidelity co-kriging surrogate model for ship hull form optimization. *Ocean Engineering*, 243:110239, 2022. ISSN 0029-8018.

- G. Lockwood, A. Chiusole, L. Gerhardt, K. Lozinskiy, D. Paul, and N. Wright. Architecture and performance of perlmutter’s 35 pb clusterstor e1000 all-flash file system. *Proceedings of the 2021 Cray User Group*, 36(23), 2021.
- Pulong Ma, Georgios Karagiannis, Bledar A. Konomi, Taylor G. Asher, Gabriel R. Toro, and Andrew T. Cox. Multifidelity computer model emulation with high-dimensional output: An application to storm surge. *Journal of the Royal Statistical Society Series C: Applied Statistics*, 71(4):861–883, 04 2022. ISSN 0035-9254.
- P. Maher and E. P. Gerber. Atmospheric model hierarchies: Connecting theory and models. *Eos*, 100, 2019.
- Ruijia Niu, Dongxia Wu, Kai Kim, Yian Ma, Duncan Watson-Parris, and Rose Yu. Multi-fidelity residual neural processes for scalable surrogate modeling. In Ruslan Salakhutdinov, Zico Kolter, Katherine Heller, Adrian Weller, Nuria Oliver, Jonathan Scarlett, and Felix Berkenkamp, editors, *Proceedings of the 41st International Conference on Machine Learning*, volume 235 of *Proceedings of Machine Learning Research*, pages 38381–38394. PMLR, 21–27 Jul 2024.
- Anthony O’Hagan. Polynomial chaos: A tutorial and critique from a statistician’s perspective. Unpublished manuscript, University of Sheffield, 2013. Submitted to SIAM/ASA Journal of Uncertainty Quantification, 2013.
- Aylar Partovizadeh, Sebastian Schöps, and Dimitrios Loukrezis. Fourier-enhanced reduced-order surrogate modeling for uncertainty quantification in electric machine design. *Engineering with Computers*, 41:2619–2639, 2025.
- Benjamin Peherstorfer, Karen Willcox, and Max Gunzburger. Survey of multifidelity methods in uncertainty propagation, inference, and optimization. *SIAM Review*, 60(3):550–591, 2018.
- Riccardo Pellegrini, Jeroen Wackers, Riccardo Broglia, Andrea Serani, Michel Visonneau, and Matteo Diez. A multi-fidelity active learning method for global design optimization problems with noisy evaluations. *Engineering with Computers*, 39:3183–3206, 2023.
- C. Perron, D. Sarojini, D. Rajaram, et al. Manifold alignment-based multi-fidelity reduced-order modeling applied to structural analysis. *Structural and Multidisciplinary Optimization*, 65:236, 2022.
- Carl Edward Rasmussen and Christopher K. I. Williams. *Gaussian Processes for Machine Learning*, volume 2. MIT Press, United States, 2006.
- T.D. Ringler, J. Thuburn, J.B. Klemp, and W.C. Skamarock. A unified approach to energy conservation and potential vorticity dynamics for arbitrarily-structured C-grids. *Journal of Computational Physics*, 229(9):3065–3090, 2010.
- O. Roderick, M. Anitescu, and Y. Peet. Proper orthogonal decompositions in multifidelity uncertainty quantification of complex simulation models. *International Journal of Computer Mathematics*, 91(4):748–769, 2014.
- A. Rosati and K. Miyakoda. A general circulation model for opper ocean simulation. *Journal of Physical Oceanography*, 18(11):1601 – 1626, 1988.

- F. Röske. An atlas of surface fluxes based on the ECMWF reanalysis. A climatological data set to force global ocean general circulation models. Technical Report 323, Max-Planck-Inst. Für Meteorol., Hamburg, Germany, 2001.
- J. Sacks, W. J. Welch, T. J. Mitchell, and H. P. Wynn. Design and analysis of computer experiments. *Statistical Science*, 4(4):409–423, 1989.
- Tapio Schneider, Shiwei Lan, Andrew Stuart, and João Teixeira. Earth system modeling 2.0. *Geophysical Research Letters*, 44(24):12,396–12,417, 2017.
- Nicholas D. Sidiropoulos, Lieven De Lathauwer, Xiao Fu, Kejun Huang, Evangelos E. Papalexakis, and Christos Faloutsos. Tensor decomposition for signal processing and machine learning. *IEEE Transactions on Signal Processing*, 65(13):3551–3582, jul 2017. ISSN 1053-587X.
- Alex J Smola and Bernhard Schölkopf. A tutorial on support vector regression. *Statistics and Computing*, 14(3):199–222, 2004.
- Jialin Song, Yuxin Chen, and Yisong Yue. A general framework for multi-fidelity bayesian optimization with gaussian processes. In *Proceedings of the Twenty-Second International Conference on Artificial Intelligence and Statistics (AISTATS)*, volume 89 of *Proceedings of Machine Learning Research*, pages 3158–3167. PMLR, April 2019.
- Julienne Stroeve and Dirk Notz. Changing state of arctic sea ice across all seasons. *Environmental Research Letters*, 13(10):103001, sep 2018.
- Ivan Sudakow, Michael Pokojovy, and Dmitry Lyakhov. Statistical mechanics in climate emulation: Challenges and perspectives. *Environmental Data Science*, 1:e16, 2022.
- S. Surjanovic and D. Bingham. Virtual library of simulation experiments: Test functions and datasets. Retrieved November 3, 2025, from <http://www.sfu.ca/~ssurjano>, 2013.
- Runshi Tang, Tamara Kolda, and Anru R. Zhang. Tensor decomposition with unaligned observations. *SIAM Journal on Matrix Analysis and Applications*, August 2025. accepted for publication.
- Ledyard R Tucker. Some mathematical notes on three-mode factor analysis. *Psychometrika*, 31(3):279–311, 1966.
- A. K. Turner, W. H. Lipscomb, E. C. Hunke, D. W. Jacobsen, N. Jeffery, D. Engwirda, T. D. Ringler, and J. D. Wolfe. MPAS-Seaice (v1.0.0): Sea-ice dynamics on unstructured Voronoi meshes. *Geoscientific Model Development*, 15(9):3721–3751, 2022.
- Adrian K. Turner and Elizabeth C. Hunke. Impacts of a mushy-layer thermodynamic approach in global sea-ice simulations using the CICE sea-ice model. *Journal of Geophysical Research: Oceans*, 120(2):1253–1275, 2015.
- Jorge Rolando Urrego-Blanco, Nathan Mark Urban, Elizabeth Clare Hunke, Adrian Keith Turner, and Nicole Jeffery. Uncertainty quantification and global sensitivity analysis of the los alamos sea ice model. *Journal of Geophysical Research: Oceans*, 121(4), 4 2016. ISSN 2169-9275.
- A. Waling, A. Herrington, K. Duderstadt, J. Dibb, and E. Burakowski. Using variable-resolution grids to model precipitation from atmospheric rivers around the greenland ice sheet. *Weather and Climate Dynamics*, 5(3):1117–1135, 2024.

- Dongxia Wu, Matteo Chinazzi, Alessandro Vespignani, Yi-An Ma, and Rose Yu. Multi-fidelity hierarchical neural processes. In *Proceedings of the 28th ACM SIGKDD Conference on Knowledge Discovery and Data Mining*, KDD '22, page 2029–2038, New York, NY, USA, 2022. Association for Computing Machinery. ISBN 9781450393850.
- J. Yi, Y. Shen, and C. A. Shoemaker. A multi-fidelity rbf surrogate-based optimization framework for computationally expensive multi-modal problems with application to capacity planning of manufacturing systems. *Structural and Multidisciplinary Optimization*, 62:1787–1807, 2020.
- Ali Zare, Alp Ozdemir, Mark A. Iwen, and Selin Aviyente. Extension of pca to higher order data structures: An introduction to tensors, tensor decompositions, and tensor pca. *Proceedings of the IEEE*, 106(8):1341–1358, 2018.